RESEARCH ARTICLE

NANO · MICRO small
www.small-journal.com

A Doping-Induced $SrCo_{0.4}Fe_{0.6}O_3/CoFe_2O_4$ Nanocomposite for Efficient Oxygen Evolution in Alkaline Media

Heng Liu, Yuan Wang, Pengfei Tan, Egon C. dos Santos, Stuart M. Holmes, Hao Li, Jun Pan,* and Carmine D'Agostino**

Perovskite and spinel oxides are promising alternatives to noble metal-based electrocatalysts for oxygen evolution reaction (OER). Herein, a novel perovskite/spinel nanocomposite comprised of $SrCo_{0.4}Fe_{0.6}O_3$ and $CoFe_2O_4$ (SCF/CF) is prepared through a simple one-step method that incorporates iron doping into a $SrCoO_{3-\delta}$ matrix, circumventing complex fabrication processes typical of these materials. At a Fe dopant content of 60%, the $CoFe_2O_4$ spinel phase is directly precipitated from the parent $SrCo_{0.4}Fe_{0.6}O_3$ perovskite phase and the number of active B-site metals (Co/Fe) in the parent SCF can be maximized. This nanocomposite exhibits a remarkable OER activity in alkaline media with a small overpotentional of 294 mV at 10 mA cm^{-2}. According to surface states analysis, the parent SCF perovskite remains in its pristine form under alkaline OER conditions, serving as a stable substrate, while the second spinel CF is covered by 5/8 monolayer (ML) O*, exhibiting considerable affinity toward the oxygen species involved in the OER. Analysis based on advanced OER microkinetic volcano model indicates that a 5/8 ML O* covered-CF is the origin for the remarkable activity of this nanocomposite. The results reported here significantly advance knowledge in OER and can boost application, scale-up and commercialisation of electrocatalytic technologies toward clean energy devices.

1. Introduction

In recent years, the development of clean and renewable energy sources has gained significant momentum due to the growing concerns about the environmental impacts of fossil fuels.[1] In this context, hydrogen (H_2) has emerged as the most promising alternative to conventional fuels, and various technologies have been proposed for its production.[2] The H_2 produced from direct steam methane reforming, steam methane reforming with carbon capture, and polymer electrolyte membrane electrolysis is commonly referred by color designations, such as gray, blue, and green, respectively.[3] Among these, water splitting presents itself as the best approach for the production of "green" hydrogen, the most pristine and sustainable source of hydrogen. Typically, water splitting consists of two half-reactions, namely the hydrogen evolution reaction (HER) occurring on the cathode and the anodic oxygen evolution reaction (OER). Compared to the cathodic HER, the anodic OER, which can be represented in alkaline media as $4OH^- \rightarrow O_2 + 2H_2O + 4e^-$, involves a kinetically sluggish four-electron process that acts as a bottleneck for the overall reaction.[4] Therefore, developing effective electrocatalysts able to speed up this process is much sought-after.

To date, the commercial catalysts for OER are still based on noble metal oxides, such as RuO_2 and IrO_2, which are expensive and

H. Liu, S. M. Holmes, C. D'Agostino
Department of Chemical Engineering
The University of Manchester
Oxford Road, Manchester M13 9PL, UK
E-mail: carmine.dagostino@manchester.ac.uk

H. Liu, Y. Wang, P. Tan, J. Pan
State Key Laboratory for Powder Metallurgy
Central South University
Changsha 410083, P. R. China
E-mail: jun.pan@csu.edu.cn

E. C. dos Santos, H. Li
Advanced Institute for Materials Research (WPI-AIMR)
Tohoku University
Sendai 980-8577, Japan
E-mail: li.hao.b8@tohoku.ac.jp

C. D'Agostino
Dipartimento di Ingegneria Civile
Chimica
Ambientale e dei Materiali (DICAM)
Alma Mater Studiorum-Università di Bologna
Via Terracini, 28, Bologna 40131, Italy

The ORCID identification number(s) for the author(s) of this article can be found under https://doi.org/10.1002/smll.202308948

DOI: 10.1002/smll.202308948

scarce.[5] These issues pose challenges to the implementation of the water splitting process on a commercial scale. As such, various transition metal oxides (TMOs), especially perovskite-[6] and spinel-type oxides,[7] have emerged as promising alternatives to noble metal-based electrocatalysts.[8]

Perovskite oxides can be generally represented as $ABO_{3\pm\delta}$, where A is a rare-earth or alkaline element while B is usually a transition metal.[4e,9] Perovskite materials possess the advantageous characteristic of providing tunable physicochemical properties due to their lattice tolerance, which enables accommodation of almost all the elements in the periodic table.[10] In this context, doping an active but non-expensive and widely available element, such as Fe, presents a feasible approach. For example, Abreu et al.[11] used a facile glycine-nitrate combustion method to fabricate a series of Fe-doped $La_{0.6}Ca_{0.4}CoO_3$ and studied the impact of B-site substitution. With the incorporation of Fe, a mixed oxidation state of Co was found which was responsible for an optimized activity indicated by a drop in the Tafel slope. Active cobalt-hydroxides[12] were found to generate on the surface, which lowered the energy barrier of rate-determination step. By density functional theory (DFT) calculations, Duan et al.[13] analyzed the impact of Fe substitution into $LaCoO_3$. The results demonstrated that the covalency behavior between Co 3d-O 2p orbitals was significantly strengthened after Fe doping, which contributed to an improved OER performance. Kim et al.[14] also found that introducing Fe into Co-based perovskites could significantly improve the catalytical performance even when the content of Fe dopant is only ~5 wt %. In addition to the doping method, constructing nanocomposites is another feasible strategy to adjust the catalytic performance of perovskite materials.[15] For instance, Rincon et al.[16] introduced Fe-N_x/C into perovskites, significantly enhancing the oxygen reduction reaction (ORR) and OER activities. Kim et al.[17] fabricated a perovskite/carbon composite material, $Sm_{0.5}Sr_{0.5}CoO_{3-\delta}$/ N-doped graphene, which exhibited a considerable activity in both ORR and OER.

Spinel oxides, with a chemical formula of AB_2O_4, have been studied as another promising alternative for precious metal-based electrocatalysts. Among numerous spinel oxides, cobalt oxides are the most competitive one for OER considering their low-cost and high-performance.[18] Fang et al.[19] reported a novel 2D ultrathin $CoFe_2O_4$ nanosheet with abundant oxygen vacancies by the treating of Prussian blue analogs. This type of Co-based spinel oxides exhibits an optimal electrochemical performance with a relatively low overpotential of 275 mV at 10 mA cm^{-2} and a Tafel slope of only 42.1 mV dec^{-1} in alkaline media. Bian et al.[20] designed a $CoFe_2O_4$/graphene nanocomposite that can act as a bi-functional electrocatalyst for ORR and OER. The performance and considerable stability of this nanohybrid were attributed to the strong coupling effect between $CoFe_2O_4$ nanoparticles and the graphene substrate. Although numerous publications have reported on the individual properties and applications of perovskite and spinel oxides, few have focused on combining these two active and affordable materials. Furthermore, in previous research efforts, doping and constructing composites for perovskite have been treated as two individual processes, potentially requiring two distinct steps to obtain an optimal perovskite-derived electrocatalyst. For instance, Hua et al.[5b] utilized electrospinning to prepare a doped perovskite oxide, $La_{0.4}5Sr_{0.45}Mn_{0.9}Fe_{0.1}O_{3-\delta}$ (LSMFO), which was subsequently modified with Fe_3C and carbon in a separate step. Notwithstanding the fact that several studies have demonstrated the feasibility of integrating these two phases into a single nanohybrid, the methodologies employed invariably entail complex fabrication processes. This complexity is counterproductive from a cost-effectiveness perspective. Therefore, a simplified one-step synthesis strategy for fabricating perovskite-derivative electrocatalysts is required. In this context, our previous work proposed a feasible strategy to generate the second phase in situ from parent perovskite phase without introducing extra steps or metal precursors.[4e] That strategy maximized the active Co metals in bulk $SrCoO_{3-\delta}$ by precipitating them onto the surface to generate the second phase, Co_3O_4, thus allowing them to be fully engaged in the reaction which can significantly improve the catalytical performance. However, the poor intrinsic activity of the Co_3O_4 second phase limits its potential for further implementation. In this respect, it is plausible to speculate that a considerable enhancement of the OER performance can be achieved if an active phase can be introduced.

Moreover, recent studies[21] have demonstrated that the surface states of TMOs under electrocatalytic conditions are generally distinct from their stoichiometric forms. Underestimating this effect will certainly mislead the analysis of reaction mechanism. Therefore, it is important to conduct surface state analysis before analyzing the structure-performance relationships.

Herein, targeting a potential second phase, an active Fe dopant is introduced into the B-site of $SrCoO_{3-\sigma}$ ($SrCo_{1-x}Fe_xO_{3-\sigma}$, x = 0, 0.2, 0.4, 0.6, 0.8, and 1) to enable spontaneous precipitation of Co and Fe. When the iron content is 60%, an active $CoFe_2O_4$ spinel phase is obtained, which achieves the doping-induced fabrication of $SrCo_{0.4}Fe_{0.6}O_3$ /$CoFe_2O_4$ (SCF/CF) nanocomposite. Both Co and Fe in parent bulk phase are maximized to be engaged into the reaction with the form of $CoFe_2O_4$, which contributes to a superior OER activity in alkaline media. This strategy not only facilitates effective integration between perovskite and spinel phases, but also achieves a simultaneous unification of doping and composite fabrication methodology in a single step. The synergetic effect between SCF and CF phases is elucidated through theoretical calculations. Surface state analysis by Pourbaix diagram calculations elucidate that the parent SCF phase will remain in its initial stoichiometric form while the generated CF will be covered by ~5/8 monolayer (ML) O* on the (110) surface. The inert adsorption behavior toward oxygen-related species observed in SCF (001) surface enables a stable substrate for the second phase, while the considerable affinity to O-related species on CF(110) makes it the origin of the overall activity.

2. Results and Discussion

2.1. Physico-Chemical Characterization

Scanning electron microscope (SEM) images of $SrCo_{1-x}Fe_xO_3$ with different Fe concentrations are displayed in **Figure 1a**. A morphology consisting of 2D nanoplates and nanoparticles can be observed. The crystal phase and elemental composition of $SrCo_{0.4}Fe_{0.6}O_3$ (when x = 0.6) are quantified by XRD and XPS, respectively. In Figure 1b, for a Fe doping content of 0.6, two distinct phases can be identified in the XRD patterns, which are the

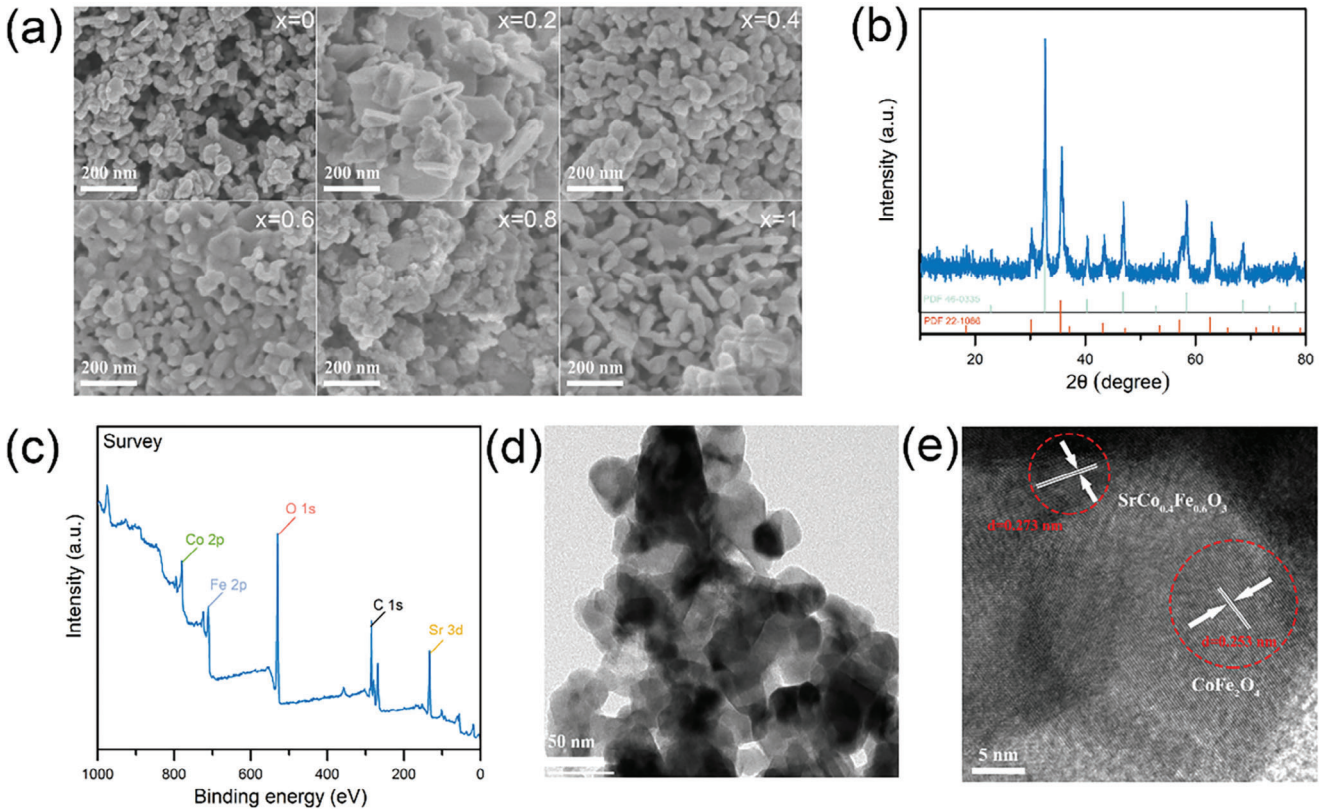

Figure 1. a) Magnified FE-SEM images of all samples with different Fe concentration, x, of 0, 0.2, 0.4, 0.6, 0.8, and 1.0. b) XRD patterns of SCF/CF. c) X-ray photoelectron spectra of SCF/CF. d) TEM images of a) SCF/CF and e) Corresponding HRTEM patterns.

$SrCo_{0.4}Fe_{0.6}O_3$ (SCF, PDF # 46-0335) perovskite phase and the $CoFe_2O_4$ (CF, PDF # 22-1086) spinel phase. This evidence proves the successful synthesis of the SCF/CF nanocomposite. The crystal phase results for other samples with varying Fe content are presented in Figure S1 (Supporting Information), indicating that these samples can maintain a single perovskite phase. The XPS results in Figure 1c demonstrate that the elemental composition (Co, Fe, Sr, and O) of SCF/CF is consistent with the XRD results. To further confirm the presence of the SCF/CF phase, transmission electron microscopy (TEM) and high-resolution transmission electron microscopy (HRTEM) analyses were performed. The morphology observed in Figure 1d is consistent with the SEM results as shown in Figure 1a. More importantly, Figure 1e reveals two distinct lattice fringes. A spacing of 0.272 nm can be attributed to the (1 1 0) lattice planes of $SrCo_{0.4}Fe_{0.6}O_3$, while the spacing of 0.253 nm corresponds to the (3 1 1) lattice planes of $CoFe_2O_4$. Detailed information on the derivation of this spacing data is provided in Figure S2, Supporting Information. These results provide strong evidence for the successful fabrication of the SCF/CF nanocomposite using the one-step method used in this work.

The valence states of SCF/CF nanocomposite are identified by XPS analysis with all the binding energy values calibrated against the C 1s peak located at 284.8 eV (Figure 1c). Detailed deconvolution results are given in **Figure** 2a–c for Co 2p, Fe 2p, and O 1s in SCF/CF, respectively. In Figure 2a, the peaks with a binding energy of 779.7 and 794.6 eV represent the existence of Co^{3+}, while peaks at 780.8 eV and 795.5 stand for Co^{4+}. This result is consistent with previous report[22] about $SrCo_{0.2}Fe_{0.8}O_{3-\delta}$. In such non-stoichiometric perovskite with inherent oxygen vacancies, the B-site metals, like Co/Fe in SCF, are likely to exhibit multiple valence states to maintain valence equilibrium within the compound. It is important to note that although the catalysts initially form oxygen vacancies during preparation, they may experience surface reconstruction when exposed to highly oxidized potentials during OER. This can lead to the oxygen re-filling into the vacancies, which was proven by our recent theoretical work[23] via surface Pourbaix computations. This phenomenon reinforces the validity of employing stoichiometric forms as the basis for structural modelling in subsequent theoretical computations. As for the peaks at 781.9 and 796.7 eV, they can be attributed to Co^{2+}.[24] The presence of divalent cobalt is a strong indicator of the existence of the second spinel $CoFe_2O_4$ phase, within which the cobalt cations are predominantly in a +2-valence state. This observation aligns with the known valency characteristics in the structure of $CoFe_2O_4$. Meanwhile, this can further verify the successful preparation of SCF/CF nanocomposite. As for Fe cations in Figure 2b, Fe^{3+} can be represented by the peaks at 710.2 and 723.4 eV, while Fe^{4+} is depicted by peaks with a binding energy of 712.5 and 725.1 eV. This results also align with previous research.[22] In the O 1s core level spectra (Figure 2c), four distinct peaks can be identified which aligns with previous studies.[25] Specifically, the peak with a binding energy of 528.1 eV is due to lattice oxygen represented by O_2^-. The peak located at 529.63 eV

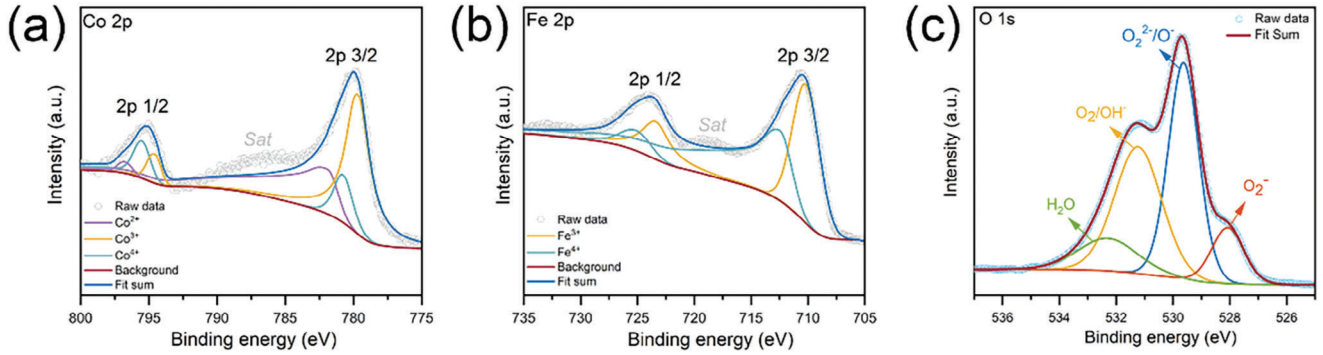

Figure 2. XPS high-resolution spectra of: a) Co 2p; b) Fe 2p; c) O 1s.

can be ascribed to O_2^{2-}/O^-, the superoxidative oxygen species. These species have been proven to be very beneficial for OER.[26] The SCF/CF nanocomposite possesses considerable content of O_2^{2-}/O^- indicating an excellent performance, which is further investigated in the theoretical study section. As for the peak at 531.2 eV, this is the signal of surface adsorbed molecular oxygen or hydroxyl groups. In addition, the O signal from molecular H_2O shows a binding energy of 532.3 eV.

2.2. Catalytic Activity Studies

The electrocatalytic activities were evaluated through linear sweep voltammetry (LSV) in a three-electrode system with 1 M KOH as reaction medium. As can be seen in **Figure 3**a,b and Figure S3 (Supporting Information), SCF/CF exhibits the best OER activity with the lowest overpotential under 10 mA cm^{-2} among all the samples investigated, including the pure $SrCo_{0.4}Fe_{0.6}O_3$ and $CoFe_2O_4$, which is only 294 mV, much lower than that of commercial RuO_2 (340 mV). For a wider comparison, a summary of the OER performances of the different perovskite oxides reported in the literature can be found in Table S1 (Supporting Information). It is clear from the comparison that the SCF/CF nanocomposite synthesised in this work ranges among the best performing materials of the perovskite families previously reported, with the advantage of having a very simple and low-cost preparation method. The Tafel plots in Figure 3c provide information on the reaction kinetics for the OER. By analysing these plots, one can extrapolate important information on the performance of the electrocatalysts (the lower the slope, the better the kinetics). It can be observed that SCF/CF exhibits the lowest Tafel slope of 64.8 mV dec^{-1}, hence the highest OER activity.

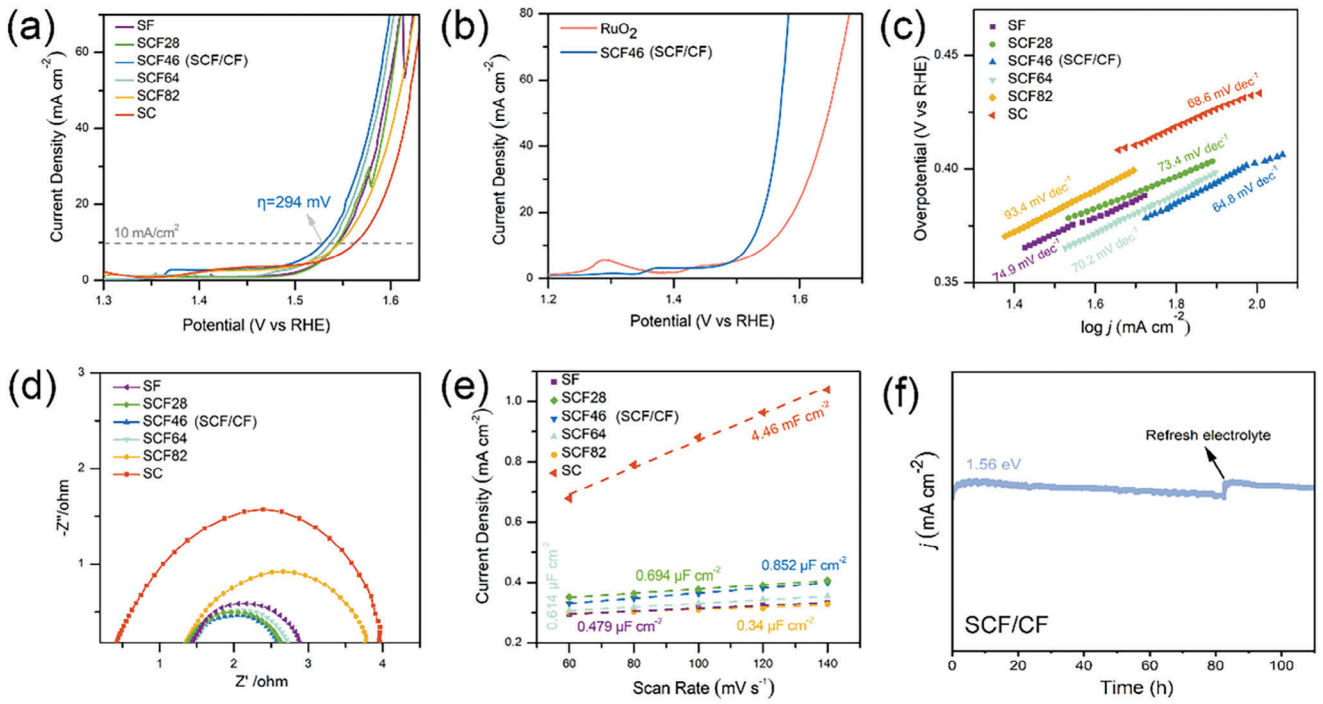

Figure 3. a) LSV curves of different samples; b) LSV curves of commercial RuO_2 and SCF/CF; c) Tafel slope of all samples; d) EIS curves; and e) double-layer capacitances (C_{dl}) of all samples with different Fe concentration; and (f) chronoamperometry curves of SCF/CF (110 h).

The charge transfer ability is another crucial factor that determines the catalytic performance. To investigate this aspect, electrochemical impedance spectroscopy (EIS) was employed to characterize the charge transfer abilities of all the catalysts studied in this work. A smaller semicircle in the EIS plot indicates a better charge transfer ability. In Figure 3d, it is evident that SCF/CF exhibits the highest charge transfer ability, further indicating its superior OER performance. Meanwhile, the impedance can also be derived from this figure. Clearly, the intersection points of each plot with the *x*-axis on the left side are different. This can further clarify the unique performance of SCF/CF when compared with other samples. Moreover, cyclic voltammetry (CV) was employed to determine the electrochemical active surface area (ECSA), which is also a critical parameter to evaluate when investigating the OER activity of a catalyst. The corresponding CV data for different Fe concentration is shown in Figure S4 (Supporting Information). More precisely, ECSA is directly proportional to the amount of the double layer capacitance C_{dl}. Interestingly, in Figure 3f, the C_{dl} of SCF/CF (0.852 μF cm^{-2}), is much lower than that of SC (4.46 mF cm^{-2}), which indicates that this nanocomposite performs well than other samples with different Fe contents. Nevertheless, based on its superior OER activity, we can rationally speculate that the ECSA is not the key factor dominating the intrinsic performance. Finally, the catalytic stability of SCF/CF in alkaline media is evaluated by chronoamperometry and the result is given in Figure 3f. SCF/CF exhibits a considerable durability for 110 h at an applied potential of 1.56 V versus RHE without obvious degradation. The morphology after this long-time durability test is examined by FE-SEM, as shown in Figure S5 (Supporting Information). Clearly, SCF/CF can retain its structure which can also clarify the considerable stability.

2.3. Theoretical Analysis

To provide more insights into the performances of the SCF/CF nanocomposite, density functional theory (DFT) calculations and microkinetic modeling were performed to analyse the origin of the superior OER activity of the material. To address the computational complexity and lattice mismatch between SCF and CF, we developed a simplified hypothesis for the nanocomposite structure by constructing two individual surface models. This approach facilitates a comprehensive understanding of the interplay between different phases within a composite structure. To note, the $SrCo_{0.375}Fe_{0.625}O_3$ (Figure S6, Supporting Information) ordered phase was used to approximate the structure of $SrCo_{0.4}Fe_{0.6}O_3$. According to our recent study,[21a] the real states of TMOs surfaces (i.e., the surface coverage and vacancy information) may significantly differ from their stoichiometric pristine forms under electrochemical working conditions. These

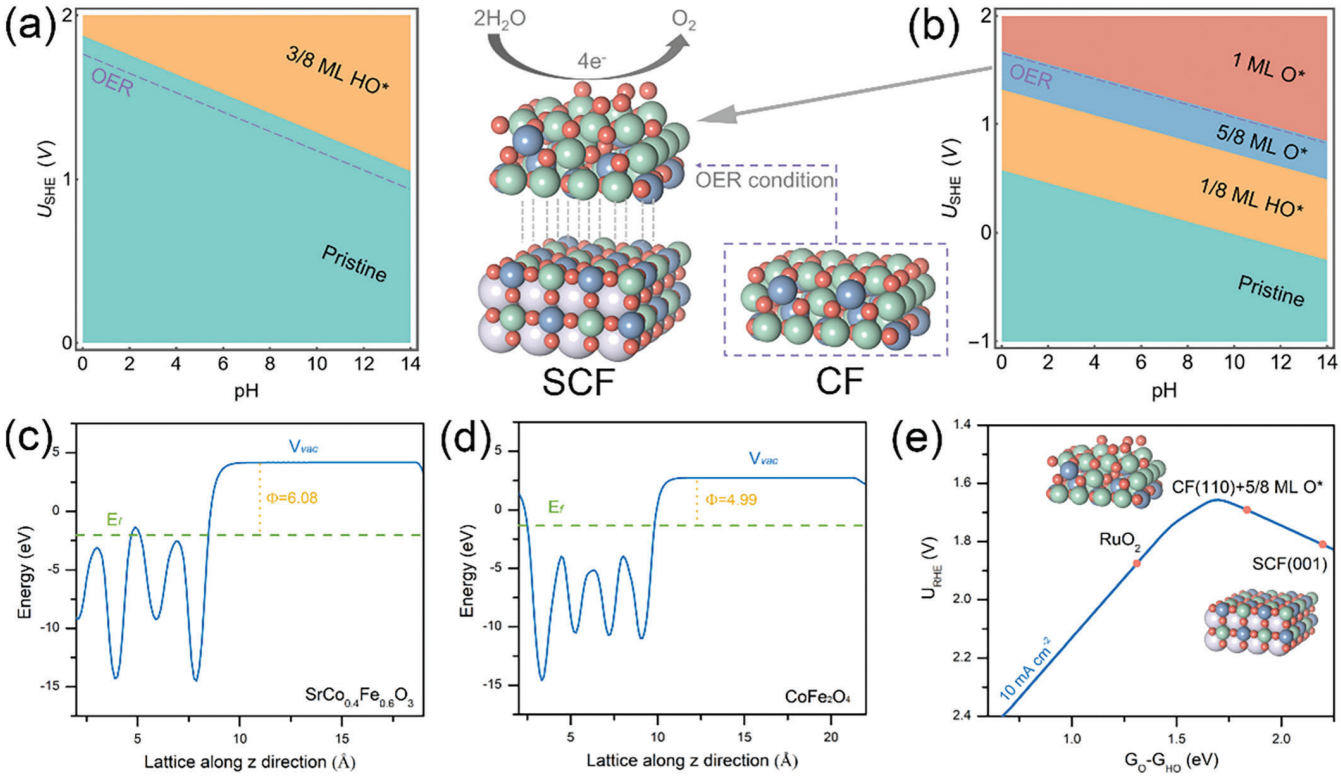

Figure 4. Calculated 2D surface Pourbaix diagrams as the function of potential (vs SHE) and pH (T = 298.15 K) for: a) SCF (001); b) CF (110). Plot of the electrostatic potential along the *z*-direction: c) SCF (001); d) CF (110) surfaces. The Fermi energy (E_f), electrostatic potential of the vacuum region (V_{vac}) and work function (Φ) are indicated. e) The derived microkinetic volcano activity model for OER. Insets are the atomic models for SCF (001), CF (110), and CF (110) covered by 5/8 ML O*. Note that the G_O−G_{HO} value for pristine CF (110) is ≈3.07 eV, which is far from the volcano peak and is not shown in this figure. The data for RuO_2 was based on the identified surface state with the result from previous work.[23] Gray, green, blue, and red spheres denote Sr, Fe, Co, and O, respectively.

differences will lead to a distinct reaction mechanism, thereby it is indispensable to conduct a computational surface state probing. The 2D surface Pourbaix diagrams are shown in **Figure** 4a,b for SCF (001) and CF (110), respectively. Under alkaline OER conditions, SCF (001) remains in its pristine form while CF (110) is covered by ~5/8 ML O*. The detailed 1D surface Pourbaix diagrams are given in (Figures S7,S8, Supporting Information). From this coverage case, the layout of this nanocomposite can be derived and is displayed in the inset. Since the parent SCF surface exhibits an inert adsorption capacity for O* and HO*, it remains a stable substrate for the second CF phase. Conversely, the CF surface exhibits a favorable adsorption behavior toward HO* and O* species, rendering it an active phase for the OER reaction. This structural layout model can be further supported by the results of work function calculations,[27] as shown in Figure 4c,d. The work function value (Φ) for CF is significantly lower than that of SCF, indicating that electrons on the CF (110) surface are more easily activated to interact with adsorbates. Combining with the observed superior OER performance of SCF/CF, it can be inferred that the CF (110) spinel phase tends to be present near the surface of this nanocomposite, which is responsible for the adsorption of intermediates. The work function of pure $SrFeO_3$ ($x = 1$) and $SrCoO_3$ ($x = 0$) are also shown in Figure S9 (Supporting Information) for comparison. We further analyze the activity of SCF (001), pristine CF (110), and CF (110) covered by 5/8 ML O* based on a state-of-the-art OER microkinetic volcano model.[28] Various possible potential-dependent kinetics and thermodynamics involving in the OER process[28,29] are considered in this model, making it more accurate than a conventional thermodynamic model. In Figure 4e, the best performance is observed for the 5/8 ML O*-covered CF(110), approaching the theoretical optimum activity of the volcano model. This conclusion suggests that the second CF spinel oxide is the active phase accounting for the superior activity of this SCF/CF nanocomposite.

3. Conclusion

In summary, a remarkably active nanocomposite comprised of $SrCo_{0.4}Fe_{0.6}O_3/CoFe_2O_4$ perovskite/spinel phases was synthesized for the first time via a simple doping-induced method. By introducing Fe into $SrCoO_{3-\sigma}$ matrix, the second $CoFe_2O_4$ spinel phase can be directly precipitated from the parent $SrCo_{0.4}Fe_{0.6}O_3$ perovskite phase (when the content of Fe dopant is 60%) without additional metal precursors. This nanocomposite shows a remarkable alkaline OER activity and stability with a small overpotential of 294 mV to reach 10 mA cm^{-2} current density and a Tafel slope of only 64.8 mV dec^{-1}. The origin of this high activity is then revealed by DFT calculations and microkinetic modeling. Firstly, by surface state probing, the parent SCF is shown to be inert for oxygen-containing species (i.e., O* and HO*), suggesting that it can act as a stable substrate accommodating second phase. Regarding the CF, this tends to be covered by ~5/8 ML O*, showing a favorable affinity for oxygen-containing species involved during OER. The work function analysis indicates that the surface electrons of CF are more easily activated to interact with the adsorbates, thereby making the second CF phase the active site for OER. Activity analysis based on the state-of-art OER microkinetic models further proves this result in which the 5/8 ML O*-covered CF exhibits an activity approaching the theoretical optimum of the model. Herein, a synergetic effect between these two phases is identified, in which the parent SCF phase as the substrate is responsible for the stability while the in situ generated CF phase accounts for its considerable OER activity. This work introduces a feasible approach to conduct theoretical investigations on complex nanocomposites, particularly those affected by lattice mismatch challenges. When facing these structural predicaments, the synergistic effects can still be effectively examined by two separate models using surface state analysis, work function computation and microkinetic investigation. Furthermore, this study demonstrates the successful integration of perovskite and spinel oxides to create a highly active and stable nanocomposite that can serve as a viable substitute for noble metal-based materials in energy-related applications.

Supporting Information

Supporting Information is available from the Wiley Online Library or from the author.

Acknowledgements

H.L. and Y.W. contributed equally to this work. The authors greatly acknowledge the financial support of the National Natural Science Foundation of China (12074435), the Science and Technology Innovation Program of Hunan Province (2021RC4001), Chinese Scholarship Council, JSPS KAKENHI (no. JP23K13703), and the Iwatani Naoji Foundation. The authors would also like to acknowledge the assistance given by Research IT and the use of the Computational Shared Facility at The University of Manchester. The authors acknowledge the Center for Computational Materials Science, Institute for Materials Research, Tohoku University, for the use of MASAMUNE-IMR (project no. 202212-SCKXX-0204) and the Institute for Solid State Physics (ISSP) at the University of Tokyo for the use of their supercomputers. C.D. would like to acknowledge the EPSRC (No. EP/V026089/1) for funding his research activities.

Conflict of Interest

The authors declare no conflict of interest.

Data Availability Statement

The data that support the findings of this study are available from the corresponding author upon reasonable request.

Keywords

density functional calculations, oxygen evolution reaction, perovskite-spinel nanocomposite, surface Pouribaix diagram

Received: November 29, 2023
Revised: November 30, 2023
Published online:

[1] a) X. Wang, H. Zhong, S. Xi, W. S. V. Lee, J. Xue, *Adv. Mater.* **2022**, *34*, 2107956; b) L. Xu, Q. Jiang, Z. Xiao, X. Li, J. Huo, S. Wang, L. Dai,

Angew. Chem. **2016**, *128*, 5363; c) J. Zhao, J.-J. Zhang, Z.-Y. Li, X.-H. Bu, *Small* **2020**, *16*, 2003916; d) X. Xie, L. Du, L. Yan, S. Park, Y. Qiu, J. Sokolowski, W. Wang, Y. Shao, *Adv. Funct. Mater.* **2022**, *32*, 2110036; e) Z. Kou, X. Li, L. Zhang, W. Zang, X. Gao, J. Wang, *Small Sci.* **2021**, *1*, 2100011; f) R. Yang, L. Mei, Y. Fan, Q. Zhang, H.-G. Liao, J. Yang, J. Li, Z. Zeng, *Nat. Protoc.* **2023**, *18*, 555.

[2] a) S. Cui, M. Li, X. Bo, *Int. J. Hydrogen Energy* **2020**, *45*, 21221; b) W. S. Feng, W. B. Pang, Y. Xu, A. M. Guo, X. H. Gao, X. Q. Qiu, W. Chen, *ChemElectroChem* **2020**, *7*, 31; c) X. Cao, Y. Han, C. Gao, Y. Xu, X. Huang, M. Willander, N. Wang, *Nano Energy* **2014**, *9*, 301.

[3] M. Hermesmann, T. E. Müller, *Prog. Energy Combust. Sci.* **2022**, *90*, 100996.

[4] a) H. A. Tahini, X. Tan, U. Schwingenschlögl, S. C. Smith, *ACS Catal.* **2016**, *6*, 5565; b) J. Kim, X. Chen, P.-C. Shih, H. Yang, *ACS Sustainable Chem. Eng.* **2017**, *5*, 10910; c) J. A. Koza, Z. He, A. S. Miller, J. A. Switzer, *Chem. Mater.* **2012**, *24*, 3567; d) J. Zhang, X. Zhao, L. Du, Y. Li, L. Zhang, S. Liao, J. B. Goodenough, Z. Cui, *Nano Lett.* **2019**, *19*, 7457; e) H. Liu, P. Tan, Q. Ma, R. Dong, A. Zhu, L. Qiao, M. Tang, E. Li, J. Pan, *J. Colloid Interface Sci.* **2019**, *557*, 103.

[5] a) H. Sun, X. Xu, Z. Hu, L. H. Tjeng, J. Zhao, Q. Zhang, H.-J. Lin, C.-T. Chen, T.-S. Chan, W. Zhou, Z. Shao, *J. Mater. Chem. A* **2019**, *7*, 9924; b) B. Hua, M. Li, J.-L. Luo, *Nano Energy* **2018**, *49*, 117; c) R. Yang, Y. Fan, L. Mei, H. S. Shin, D. Voiry, Q. Lu, J. Li, Z. Zeng, *Anti-Cancer Drugs: Nat., Synth. Cell* **2023**, *2*, 101; d) Y. Zhang, R. Yang, H. Li, Z. Zeng, *Small* **2022**, *18*, 2203759.

[6] a) G. Ou, C. Yang, Y. Liang, N. Hussain, B. Ge, K. Huang, Y. Xu, H. Wei, R. Zhang, H. Wu, *Small Methods* **2019**, *3*, 1800279; b) Y. Zhu, W. Zhou, Z. Shao, *Small* **2017**, *13*, 1603793; c) M.-J. Choi, L. Wang, K. A. Stoerzinger, S.-Y. Chung, S. A. Chambers, Y. Du, *Adv. Energy Mater.* **2023**, *13*, 2300239; d) H. Guo, Y. Yang, G. Yang, X. Cao, N. Yan, Z. Li, E. Chen, L. Tang, M. Peng, L. Shi, S. Xie, H. Tao, C. Xu, Y. Zhu, X. Fu, Y. Pan, N. Chen, J. Lin, X. Tu, Z. Shao, Y. Sun, *ACS Catal.* **2023**, *13*, 5007.

[7] a) Z.-F. Huang, J. Song, Y. Du, S. Xi, S. Dou, J. M. V. Nsanzimana, C. Wang, Z. J. Xu, X. Wang, *Nat. Energy* **2019**, *4*, 329; b) Z. Wang, J. Huang, L. Wang, Y. Liu, W. Liu, S. Zhao, Z.-Q. Liu, *Angew. Chem.* **2022**, *134*, 202114696; c) R. Wei, X. Bu, W. Gao, R. A. B. Villaos, G. Macam, Z.-Q. Huang, C. Lan, F.-C. Chuang, Y. Qu, J. C. Ho, *ACS Appl. Mater. Interfaces* **2019**, *11*, 33012; d) Y. Zhou, S. Sun, C. Wei, Y. Sun, P. Xi, Z. Feng, Z. J. Xu, *Adv. Mater.* **2019**, *31*, 1902509.

[8] W. T. Hong, M. Risch, K. A. Stoerzinger, A. Grimaud, J. Suntivich, Y. Shao-Horn, *Energy Environ. Sci.* **2015**, *8*, 1404.

[9] a) N.-T. Suen, S.-F. Hung, Q. Quan, N. Zhang, Y.-J. Xu, H. M. Chen, *Chem. Soc. Rev.* **2017**, *46*, 337; b) Z. Shui, H. Tian, S. Yu, H. Xiao, W. Zhao, X. Chen, *Sci. China Mater.* **2022**, *66*, 1002.

[10] a) J. T. Mefford, X. Rong, A. M. Abakumov, W. G. Hardin, S. Dai, A. M. Kolpak, K. P. Johnston, K. J. Stevenson, *Nat. Commun.* **2016**, *7*, 11053; b) X. Huang, G. Zhao, G. Wang, J. T. S. Irvine, *Chem. Sci.* **2018**, *9*, 3623; c) H. Liu, X. Ding, L. Wang, D. Ding, S. Zhang, G. Yuan, *Electrochim. Acta* **2018**, *259*, 1004; d) C. Lim, C. Kim, O. Gwon, H. Y. Jeong, H.-K. Song, Y.-W. Ju, J. Shin, G. Kim, *Electrochim. Acta* **2018**, *275*, 248; e) R. Mandal, Y. Mahton, C. Sowjanya, K. Sanket, S. K. Behera, S. K. Pratihar, *J. Solid State Chem.* **2023**, *317*, 123668.

[11] M. A. Abreu-Sepulveda, C. Dhital, A. Huq, L. Li, C. A. Bridges, M. P. Paranthaman, S. R. Narayanan, D. J. Quesnel, D. A. Tryk, A. Manivannan, *J. Electrochem. Soc.* **2016**, *163*, F1124.

[12] Z. J. Xu, *Sci. China Mater.* **2019**, *63*, 3.

[13] Y. Duan, S. Sun, S. Xi, X. Ren, Y. Zhou, G. Zhang, H. Yang, Y. Du, Z. J. Xu, *Chem. Mater.* **2017**, *29*, 10534.

[14] B.-J. Kim, E. Fabbri, D. F. Abbott, X. Cheng, A. H. Clark, M. Nachtegaal, M. Borlaf, I. E. Castelli, T. Graule, T. J. Schmidt, *J. Am. Chem. Soc.* **2019**, *141*, 5231.

[15] a) Y. Zhu, W. Zhou, Z. Shao, *Small* **2017**, *13*, 1603793; b) H. Guo, Y. Yang, G. Yang, X. Cao, N. Yan, Z. Li, E. Chen, L. Tang, M. Peng, L. Shi, S. Xie, H. Tao, C. Xu, Y. Zhu, X. Fu, Y. Pan, N. Chen, J. Lin, X. Tu, Z. Shao, Y. Sun, *ACS Catal.* **2023**, *13*, 5007.

[16] R. A. Rincón, J. Masa, S. Mehrpour, F. Tietz, W. Schuhmann, *Chem. Commun. (Camb.)* **2014**, *50*, 14760.

[17] Y. Bu, G. Nam, S. Kim, K. Choi, Q. Zhong, J. Lee, Y. Qin, J. Cho, G. Kim, *Small* **2018**, *14*, e1802767.

[18] T. Maiyalagan, K. A. Jarvis, S. Therese, P. J. Ferreira, A. Manthiram, *Nat. Commun.* **2014**, *5*, 3949.

[19] H. Fang, T. Huang, D. Liang, M. Qiu, Y. Sun, S. Yao, J. Yu, M. M. Dinesh, Z. Guo, Y. Xia, S. Mao, *J. Mater. Chem. A* **2019**, *7*, 7328.

[20] W. Bian, Z. Yang, P. Strasser, R. Yang, *J. Power Sources* **2014**, *250*, 196.

[21] a) H. Liu, X. Jia, A. Cao, L. Wei, C. D'Agostino, H. Li, *J. Chem. Phys.* **2023**, *158*, 124705; b) B. R. Wygant, K. Kawashima, C. B. Mullins, *ACS Energy Lett.* **2018**, *3*, 2956.

[22] Y. Qiu, H. Li, Y. Liu, B. Chi, J. Pu, J. Li, *J. Alloys Compd.* **2020**, *829*, 154503.

[23] H. Liu, X. Jia, A. Cao, L. Wei, C. D'agostino, H. Li, *J. Chem. Phys.* **2023**, *158*, 124705.

[24] H. Guo, Y. Yang, G. Yang, X. Cao, N. Yan, Z. Li, E. Chen, L. Tang, M. Peng, L. Shi, S. Xie, H. Tao, C. Xu, Y. Zhu, X. Fu, Y. Pan, N. Chen, J. Lin, X. Tu, Z. Shao, Y. Sun, *ACS Catal.* **2023**, *13*, 5007.

[25] a) J. Bao, X. Zhang, B. Fan, J. Zhang, M. Zhou, W. Yang, X. Hu, H. Wang, B. Pan, Y. Xie, *Angew. Chem. Int. Ed. Engl.* **2015**, *54*, 7399; b) B. Hua, M. Li, Y.-F. Sun, Y.-Q. Zhang, N. Yan, J. Chen, T. Thundat, J. Li, J.-L. Luo, *Nano Energy* **2017**, *32*, 247.

[26] a) S. Liu, H. Luo, Y. Li, Q. Liu, J.-L. Luo, *Nano Energy* **2017**, *40*, 115; b) Y. Zhu, W. Zhou, J. Sunarso, Y. Zhong, Z. Shao, *Adv. Funct. Mater.* **2016**, *26*, 5862.

[27] R. Tran, X.-G. Li, J. H. Montoya, D. Winston, K. A. Persson, S. P. Ong, *Surf. Sci.* **2019**, *687*, 48.

[28] C. F. Dickens, C. Kirk, J. K. Nørskov, *J. Phys. Chem. C* **2019**, *123*, 18960.

[29] a) S. Pan, H. Li, D. Liu, R. Huang, X. Pan, D. Ren, J. Li, M. Shakouri, Q. Zhang, M. Wang, C. Wei, L. Mai, B. Zhang, Y. Zhao, Z. Wang, M. Graetzel, X. Zhang, *Nat. Commun.* **2022**, *13*, 2294; b) Y. Zhu, X. Wang, X. Zhu, Z. Wu, D. Zhao, F. Wang, D. Sun, Y. Tang, H. Li, G. Fu, *Small* **2023**, *19*, 2206531.